Volume 8
Number 9
7 May 2020
Pages 2331-2704

Biomaterials Science

rsc.li/biomaterials-science

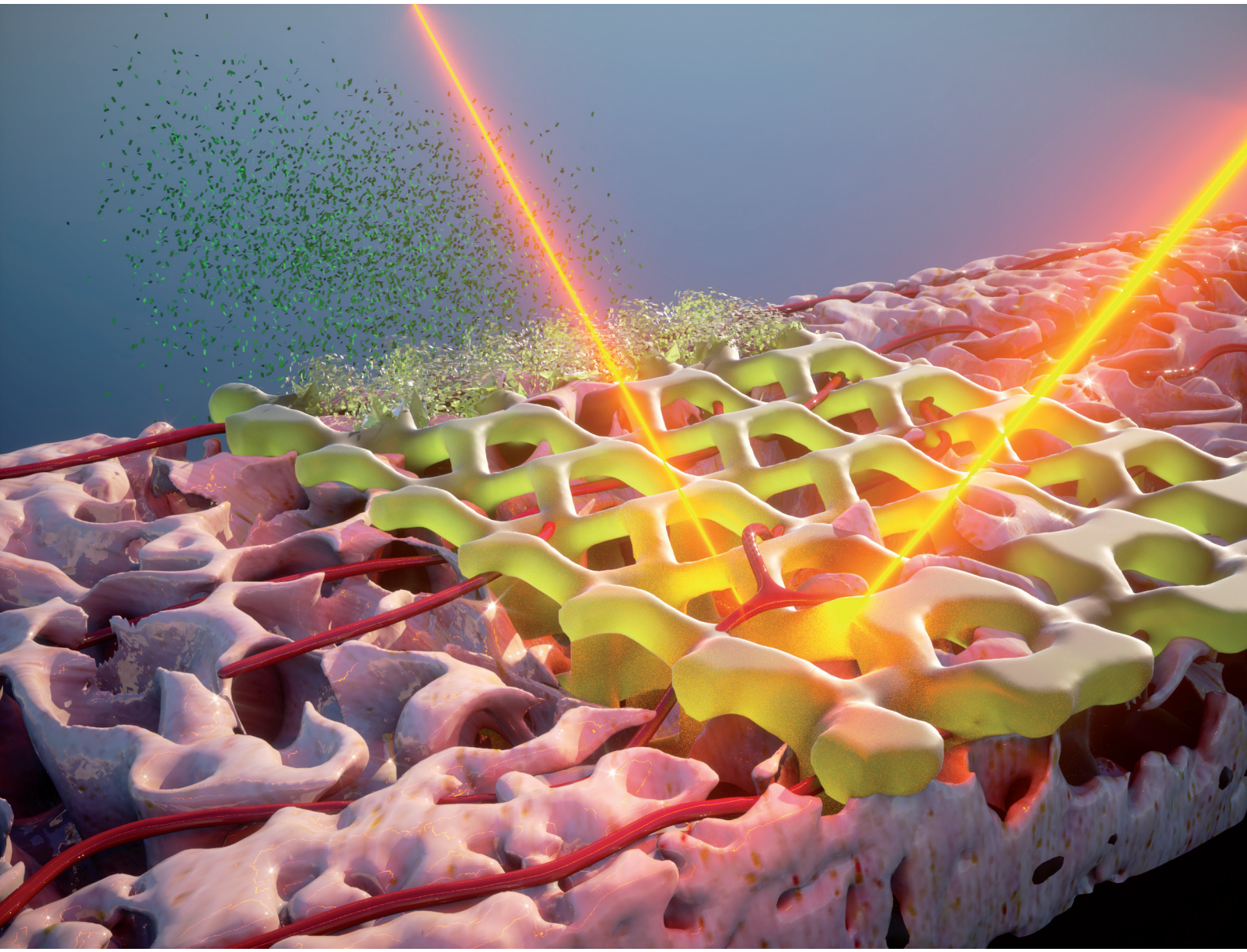

ISSN 2047-4849

ROYAL SOCIETY OF CHEMISTRY

PAPER
Y. Li *et al.*
Additively manufactured functionally graded biodegradable porous zinc

European Society for Biomaterials

Biomaterials Science

ROYAL SOCIETY OF CHEMISTRY

PAPER

View Article Online
View Journal | View Issue

Cite this: *Biomater. Sci.*, 2020, **8**, 2404

Additively manufactured functionally graded biodegradable porous zinc

Y. Li, *[a] P. Pavanram,[b] J. Zhou,[a] K. Lietaert,[c,d] F. S. L. Bobbert,[a] Yusuke Kubo,[b] M. A. Leeflang,[a] H. Jahr†[b,e] and A. A. Zadpoor†[a]

Topological design provides additively manufactured (AM) biodegradable porous metallic biomaterials with a unique opportunity to adjust their biodegradation behavior and mechanical properties, thereby satisfying the requirements for ideal bone substitutes. However, no information is available yet concerning the effect of topological design on the performance of AM porous zinc (Zn) that outperforms Mg and Fe in biodegradation behavior. Here, we studied one functionally graded and two uniform AM porous Zn designs with diamond unit cell. Cylindrical specimens were fabricated from pure Zn powder by using a powder bed fusion technique, followed by a comprehensive study on their static and dynamic biodegradation behaviors, mechanical properties, permeability, and biocompatibility. Topological design, indeed, affected the biodegradation behavior of the specimens, as evidenced by 150% variations in biodegradation rate between the three different designs. After *in vitro* dynamic immersion for 28 days, the AM porous Zn had weight losses of 7–12%, relying on the topological design. The degradation rates satisfied the desired biodegradation time of 1–2 years for bone substitution. The mechanical properties of the biodegraded specimens of all the groups maintained within the range of those of cancellous bone. As opposed to the trends observed for other biodegradable porous metals, after 28 days of *in vitro* biodegradation, the yield strengths of the specimens of all the groups (σ_y = 7–14 MPa) increased consistently, as compared to those of the as-built specimens (σ_y = 4–11 MPa). Moreover, AM porous Zn showed excellent biocompatibility, given that the cellular activities in none of the groups differed from the Ti controls for up to 72 h. Using topological design of AM porous Zn for controlling its mechanical properties and degradation behavior is thus clearly promising, thereby rendering flexibility to the material to meet a variety of clinical requirements.

Received 26th November 2019,
Accepted 19th January 2020

DOI: 10.1039/c9bm01904a

rsc.li/biomaterials-science

1. Introduction

For bone tissue substitution, additively manufactured (AM) biodegradable porous metals are a group of the most attractive candidates,[1] as they possess several unique properties, including biodegradation, arbitrarily adjustable pore size and porosity, fully interconnected pores, and bone-mimicking mechanical properties that are multiple orders of magnitude higher than those of biodegradable polymers.[2] Ideally, the biodegradation profile of a biomaterial should match the rate of *de novo* tissue regeneration so as to maintain its mechanical integrity during the healing process while ensuring that the biomaterial disappears afterwards, paving the way for full regeneration of large bony defects.[3] Furthermore, the scaffolds should have fully interconnected pores with favorable shapes to facilitate cell proliferation, migration, and differentiation.[4]

Recently, several studies on directly printed topologically ordered porous biodegradable magnesium (Mg) and iron (Fe) have been reported[5,6] and these studies addressed some of the most important challenges faced in designing such biomaterials. For Mg- and Fe-based biomaterials, the most important challenge concerns biodegradation rate, which is too high for Mg,[7,8] but too low for Fe.[9] AM facilitates the production of porous Fe with greatly increased surface area and this can increase its biodegradation rate (0.2 mm per year (ref. 10)) to the desired range (0.2–0.5 mm per year (ref. 11)). However, according to *in vivo* tests with pure Fe, voluminous biodegradation products often form and remain in the human body even until 9 months after implantation.[12]

[a]*Department of Biomechanical Engineering, Delft University of Technology, Delft 2628 CD, The Netherlands. E-mail: y.li-7@tudelft.nl; Tel: +31-15-2786780*
[b]*Department of Anatomy and Cell Biology, University Hospital RWTH Aachen, Aachen 52074, Germany*
[c]*3D Systems - LayerWise NV, Grauwmeer 14, Leuven 3001, Belgium*
[d]*Department of Materials Engineering, KU Leuven, Kasteelpark Arenberg 44, Leuven 3001, Belgium*
[e]*Department of Orthopedic Surgery, Maastricht UMC+, Maastricht 6202 AZ, The Netherlands*
†Authors contributed equally to the study.

Some researchers have tried to adjust the biodegradation rates of Mg and Fe through the development of new alloys and functional coatings.[13,14] However, only limited adjustments in biodegradation rate are possible through these approaches. An alternative approach that has recently received a lot of attention is the use of other biodegradable metals. Within this paradigm, Zn and Zn-based alloys are considered promising candidates for orthopedic applications, as they are capable of tackling some of the fundamental challenges associated with using biodegradable Mg or Fe as an implant material.[15] Zn offers multiple advantages over Mg, Fe, and their alloys. First, as the chemical potential of Zn falls between the chemical potential values of Mg and Fe, it is expected to exhibit an intermediate rate of biodegradation, as compared to the extreme cases of Mg and Fe.[16–19] Second, the biodegradation process of Zn does not generate hydrogen gas. Finally, similar to Mg but unlike Fe, the biodegradation products of Zn are biocompatible.[20] A few research groups, including ours, have recently been successful in directly printing AM porous Zn.[21–23] In a previous study, we assessed the biodegradation behavior, mechanical properties, and cytocompatibility of an AM porous Zn biomaterial with a regular and uniform porous structure.[24]

Now, the next step is to go beyond the uniform lattice structure and fully exploit the advantages of topological design and free-form fabrication offered by AM to meet the design requirements of biodegradable porous metals aimed at applications as bone substitutes. Functionally graded designs are particularly interesting in this context, as they enable meeting conflicting design requirements in a single piece of material. Indeed, a recent study has shown that functional gradients could be used to adjust the biodegradation profile as well as the mechanical properties of AM porous Fe[10] to meet otherwise conflicting design requirements regarding biodegradation rate, mechanical properties, and permeability of such a biomaterial. It is therefore interesting to investigate if topological design can also tune the properties of other AM biodegradable porous metals.

Here, we designed and directly printed three experimental groups of AM porous Zn specimens, including one group with a functionally graded design and two groups with uniform designs to investigate the influence of topological design on the static and dynamic biodegradation behaviors, mechanical properties, permeability, and cytocompatibility of pure Zn prepared by using a powder bed fusion (PBF) technique. To put this into perspective, the porosity of the functionally graded porous structure design falls within the porosities of the two uniform porous structure designs.

2. Materials and methods

2.1. Design and AM of the specimens

Element (nTopology, USA) was used to design three different types of specimens (Fig. 1) all with a 1.4 mm diamond unit cell, which included two uniform structures (strut thicknesses: 0.3 and 0.4 mm, hereafter called S03 and S04, respectively), and a functionally graded porous structure (strut thickness: linearly and radially varied from 0.4 mm to 0.2 mm) (S0402) (Fig. 1). Specimens were fabricated using a ProX DMP 320 machine (3D Systems, Belgium) with a maximum laser power of 500 W and <50 ppm oxygen levels in its build chamber. The working pressure inside the chamber filled with argon gas was set to 150 mbar. The Zn powder was nitrogen-atomized and had the following characteristics: particle sizes: D_{10}: 26 μm, D_{50}: 39 μm, and D_{90}: 60 μm; O content: 2551 ± 81 ppm, N content: 17 ± 2 ppm, and H content: 7.6 ± 0.8 ppm.[25] The powder layer thickness and energy density were 60 μm and 39.0 J mm^{-3}, respectively. The specimens were removed from the steel baseplate through wire electrical discharge machining (WEDM). 96% ethanol was used to ultrasonically clean the unmelted powders stuck in the pores of the specimens for 20 min. Subsequently, the specimens were cleaned chemically for 2 min in 5% (by volume) HCl, 5% HNO_3, and 90% C_2H_5OH to further remove loose powder particles. Afterwards, residual HCl on the specimens were washed out by 5 min ultrasonic cleaning in 96% ethanol.

2.2. Morphological characterization of the as-built specimens

The specimens were imaged using micro-computed tomography (micro-CT) (Phoenix Nanotom, GE Sensing Inspection Technologies GmbH, Germany) at a tube voltage of 130 kV and a tube current of 220 μA. The exposure time was 500 ms and the spatial resolution was 12 μm^3. 1440 projections were acquired. The acquired data were then reconstructed and transformed to 2D images (DICOM stack) using Phoenix Datos|x 2.0 (GE Sensing & Inspection Technologies GmbH, Germany). To extract quantifiable data from these images, the following steps were taken. First, the images were imported to the Fiji software (NIH, US) and thresholded locally over a range of 107 to 255. Then, a series of circular regions of interest (ROIs) were created and porosity, strut size, and pore size were calculated using BoneJ (a plugin of Fiji).[6] Besides, the porosity of the specimens was also determined by using the weighing method.[5]

2.3. Static and dynamic biodegradation tests

A standard cell culture incubator (20% O_2, 5% CO_2, 37 °C) was used for static *in vitro* biodegradation tests in revised simulated body fluid (r-SBF),[26] for up to 28 days. In addition, dynamic *in vitro* biodegradation was performed at a flow rate of 0.3 ml min^{-1}, for the same period and also at cell culture conditions, using a custom-built bioreactor and pre-equilibrated r-SBF. Medium pH values were registered (InLab Expert Pro-ISM, METTLER TOLEDO, Switzerland) after static and dynamic biodegradation. An inductively coupled plasma optical emission spectroscope (ICP-OES, iCAP 6500 Duo, Thermo Scientific, USA) was used to analyze the concentrations of Zn, P, and Ca ions.

2.4. Characterization of the biodegradation products

Scanning electron microscope (SEM) and energy-dispersive X-ray spectroscope (EDS) (JSM-IT100, JEOL, Japan) was used to

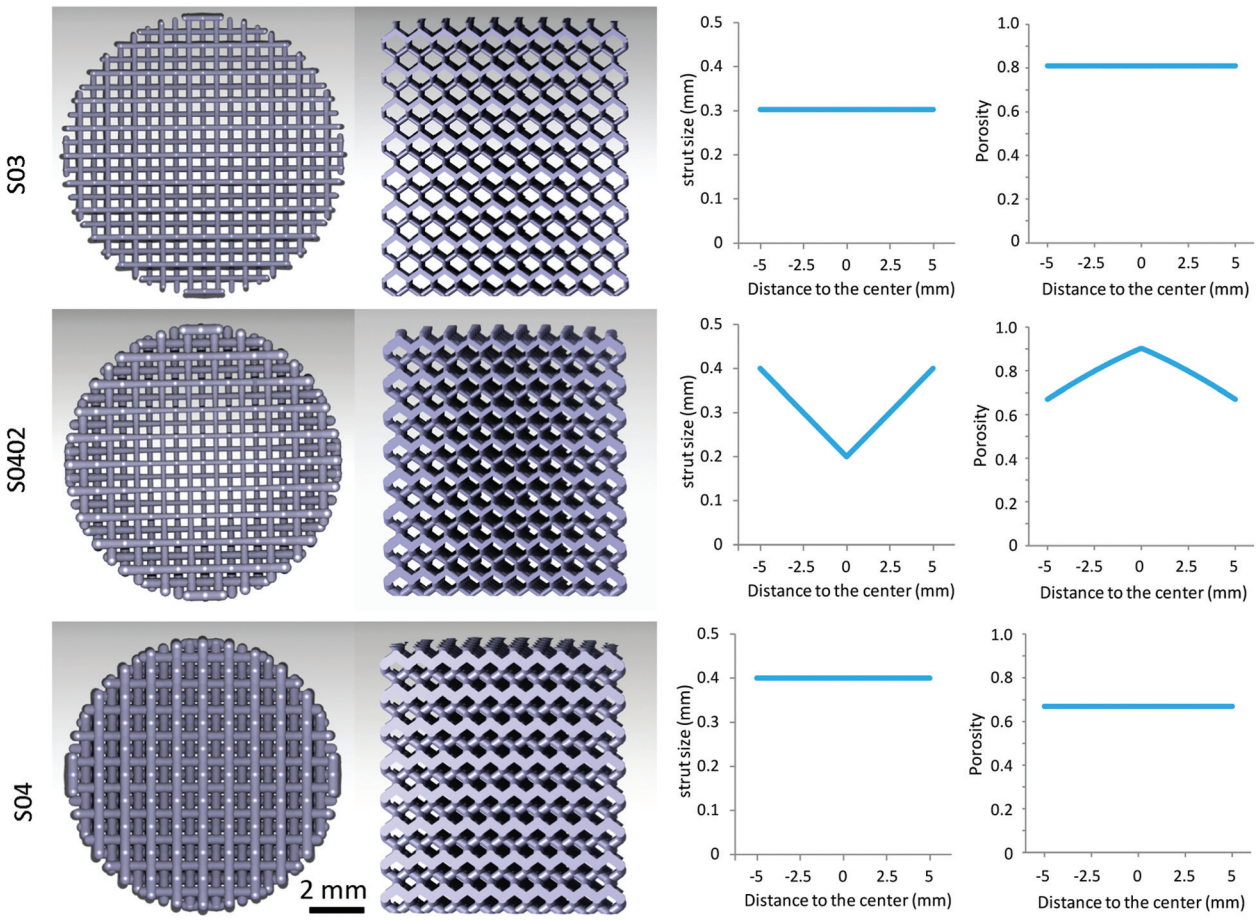

Fig. 1 Topological designs of the AM porous Zn of the three experimental groups.

analyze the morphologies and compositions of the biodegradation products. X-ray diffractometer (XRD, Bruker D8 Advance diffractometer in Bragg–Brentano geometry, Germany) was used for the identification of the phases in the biodegradation products. XRD was operated at 45 kV and 35 mA using Co Kα radiation (step size: 0.035° and dwell time: 4 s).

2.5. Morphological characterization of the specimens after biodegradation

After the biodegradation tests, ranges of 45–107 and 107–255 were applied to segment the biodegradation products and Zn, respectively, from the micro-CT images. After segmentation in Fiji, the volume of metallic specimen (*i.e.*, Zn) and the volume of the biodegradation products were calculated with BoneJ (a plugin of Fiji). The images were then imported to Avizo Fire (VSG, France) for 3D reconstruction.

2.6. Mechanical characterization

Compression tests were carried out at a crosshead speed of 2 mm min^{-1}, using a material testing machine with a 10 kN load cell (Instron, Germany). Yield strengths and quasi-elastic gradients (elastic modulus) of the specimens were obtained according to ISO 13314:2011. The slope of the starting linear part of the stress–strain curve equals to the elastic modulus of the porous specimen. The initial linear part was offset by 0.2% to find the intersection for yield strength. All the tests were performed in triplicate.

2.7. Permeability

The falling head method was used to measure the permeability of the specimens.[10] The specimens were placed in a chamber below a standpipe. Water fell in the standpipe, during which the pressure at the bottom of the standpipe was measured by a pressure gauge. Water pressure was registered in LabView (v.11.0, National Instruments, US) every two seconds. The instantaneous level of the water corresponded to the measured pressure. The following equation was used to calculate permeability, k:

$$k = \frac{a}{A}\frac{L}{t}\ln\frac{H_1}{H_2}\frac{\mu}{\rho g}$$

where a and A are the areas of the cross-section for the standpipe and specimen, respectively, L is the specimen height, H_1 and H_2 are the momentary level of water at two different time points, t is the interval between these two time points, μ is the

dynamic viscosity, and ρ is the density of water. The tests were performed in triplicate for each of the groups.

2.8. Cell seeding efficiency

Cleaned Zn scaffolds (n = 3) were sterilized in 100% isopropanol (Merck; Darmstadt, Germany) for 30 min and placed in non-tissue culture treated 48-well plates so as to achieve diminished adhesion and proliferation of cells on the surface of the wells. Cell suspension (500 μl with 3×10^6 cells) of MG-63 was prepared and added dropwise to the scaffolds. After 30 min of incubation, 1 ml of additional medium was slowly added and the specimens were further incubated for 6 h under static physiological conditions, thus, ensuring complete cell attachment. After 6 h, the scaffolds were moved to a fresh 48-well plate and a counting chamber method was used to count the remaining cells in each well.[27] The equation below was used to calculate the cell seeding efficiency:

$$\text{Cell seeding efficiency} = \frac{(\text{initial cells added to scaffold} - \text{remaining cells in wells})}{\text{initial cells added to scaffold}}.$$

2.9. Cytocompatibility

2.9.1. Cell culture. Human osteoblast-like cells (MG-63, ATCC, CRL-1427) were cultured in Dulbecco's Modified Eagle Medium (DMEM) with low (1 g L^{-1}) glucose (DMEM LG; Sigma-Aldrich Chemie GmbH, Munich, Germany), containing 10% fetal calf serum (DMEM LG+, PAN-Biotech, Aidenbach, Germany), in the incubator (37 °C, 20% O_2, 5% CO_2, and 95% humidity).

2.9.2. Cytocompatibility testing. Specimens were cleaned as reported in subsection 2.1, and then sterilized in 100% isopropanol (Merck; Darmstadt, Germany) for 30 min. The biocompatibility of the AM porous Zn specimens was subsequently evaluated through direct cell seeding and indirect extract-based cytotoxicity tests.

(a) Direct cell seeding. The cleaned and sterilized specimens were seeded with 3×10^6 MG-63 cells and incubated for 24 h in DMEM LG+ medium under physiological conditions. The specimens after cell seeding were then cut longitudinally by using a Goldsmith precision saw with hardened jewelers saw blade to evaluate cell viability in their core region using Live and Dead Dye from Live and Dead Cell Assay kit (ab115347, Abcam, UK). Briefly, a 5× concentrated dye solution was added to the cell-seeded specimens and then incubated for 10 min at room temperature, prior to fluorescent optical imaging of living cells. After rinsing in 1× phosphate buffered saline, the scaffolds were fixed, dehydrated, and air-dried at room temperature as described before.[5] SEM (ESEM XL 30 FEG, FEI, Eindhoven, The Netherlands) was used to observe the cells.

(b) Indirect, extract-based cytocompatibility. The methodology for extract preparation and the MTS assay were both previously reported by us.[6] Briefly, extracts were prepared at 0.2 g Zn ml^{-1} in DMEM LG+ for 72 h under physiological conditions as recommended by EN ISO standards 10993-5 and 10993-12. The sterile filtered (0.2 μm) extracts from Zn specimens and those from identically designed Ti-6Al-4V specimens as gold standard, were compared to cytotoxic Dimethyl sulfoxide (DMSO, 20% v/v): MG-63 cells were seeded on regular bioplastics and DMEM LG+ was replaced with 10× extracts prior to further incubation for 0, 24, 48 and 72 h. Relative cellular activity was determined using CellTiter 96® AQueous One Solution Cell Proliferation Assay (Promega Corp., Mannheim, Germany) as described by us before.[6]

2.10. Statistical analysis

One-way ANOVA tests (α = 0.05) were performed to analyze biodegradation and permeability data. Two-way ANOVA tests (α = 0.05), followed by the Turkey multiple comparison test (α = 0.05), were used to analyze cytotoxicity data ($p < 0.0001$, ****; $p < 0.001$, ***; $p < 0.01$, **; $p < 0.05$, *; n.s. = not significant).

3. Results

3.1. Morphological characteristics of the as-built specimens

The strut sizes of the AM Zn scaffolds were 40–50 μm thicker, while the pore sizes were 50–80 μm narrower than the design values (Table 1). The measured porosities were similar from μCT and the weighing method, which were 5–9% lower than the design values (Table 1). The 3D models reconstructed from the micro-CT (Fig. 2a–c) and SEM images (Fig. 2d–i) showed uniform strut thickness of the S03 and S04 groups, while the strut thickness of the S0402 group was graded. There were unmelted powder particles on the surface of the as-built specimens (Fig. 2d–f). After chemical polishing, the surfaces of the specimens were relatively smooth (Fig. 2g–i).

3.2. *In vitro* biodegradation behavior

During both the static and dynamic immersion tests, white biodegradation products formed gradually on the struts surfaces of the scaffolds of all the three experimental groups (Fig. 3a). The dynamic biodegradation appeared to produce more biodegradation products than the static one. Furthermore, the biodegradation products mainly formed at the bottom of the specimens (attached to the beaker) under the static condition, but at the top of the specimens (*i.e.*, outlet side of the medium flow) under the dynamic condition (Fig. 3a).

The pH values slightly increased from 7.5 to 7.9 in r-SBF solution during 28 days of immersion (Fig. 3b). The dynamic tests resulted in higher pH values, as compared to the static ones, especially at day 28 (Fig. 3b). pH value did not vary much

Table 1 Morphological characterization of AM porous Zn

AM porous Zn	Porosity (%)		Strut size (μm)		Pore size (μm)	
	μCT	Design	μCT	Design	μCT	Design
S03	72.6 ± 2.3	81.1	349 ± 9	300	612 ± 3	700
S0402	68.5 ± 2.3	74.3	357 ± 18	400–200	589 ± 69	600–800
S04	62.0 ± 2.5	67.4	442 ± 1	400	550 ± 38	600

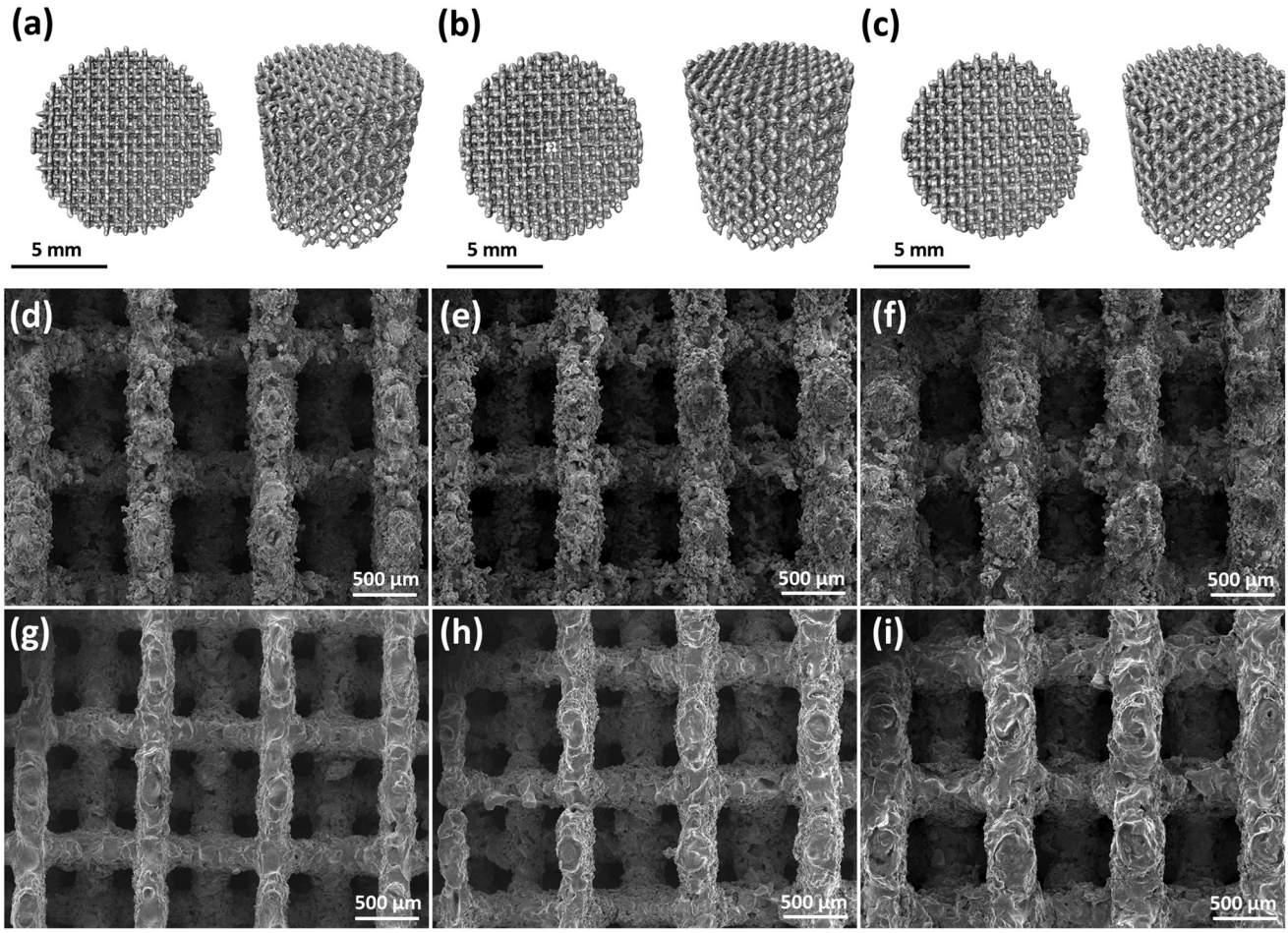

Fig. 2 Morphologies of AM porous Zn: (a–c) micro-CT reconstructions of AM porous Zn S03 (a), S0402 (b), and S04 (c), (d–f) strut morphologies of the as-built AM porous Zn S03 (d), S0402 (e), and S04 (f), (g–i) strut morphologies of the as-cleaned AM porous Zn S03 (g), S0402 (h), and S04 (i).

between the solutions with the specimens of the different groups (Fig. 3b). The static testing resulted in low Zn ion concentrations (around 0.3 mg L^{-1}) in all the three groups, even after 28 days of immersion (Fig. 3c). In contrast, the dynamic testing greatly increased the released Zn ion concentrations after day 7 (Fig. 3c). As compared to the S04 and S0402 groups, specimens of the group S03 released more Zn ions into r-SBF (Fig. 3c). After 28 days, P and Ca ion concentrations gradually decreased, respectively, to 2 mg L^{-1} and 80 mg L^{-1} (Fig. 3d and e). Similarly, the concentrations of P and Ca ions reduced to different extents under the static and dynamic conditions, with the dynamic tests always exhibiting lower P and Ca ion concentrations in the medium (Fig. 3d and e). After 28 days, specimens of the group S04 showed a lower P concentration as compared to the specimens of the groups S03 and S0402, while the variations in Ca ion concentration with immersion time did not show clear differences between the experimental groups (Fig. 3e).

3.3. Characteristics of the biodegradation products

For all the three groups, after 28 day static or dynamic degradation, four types of biodegradation products were found on the surfaces of the Zn scaffolds (Fig. 4a–f). Clusters of small particles (Fig. 4c) were mainly found on the biodegraded surfaces and contained Zn, O, C, P, and Ca. The morphological features of the other biodegradation products were: dome-like biodegradation products (Fig. 4d) that had Zn, C, O, and P, needle-like biodegradation products (Fig. 4e) that contained Zn, O, Ca, and P, and flake-like biodegradation products (Fig. 4f) that contained Zn, O, Cl, and C. XRD analysis showed the presence of ZnO, $Zn_5(CO_3)_2(OH)_6$, $Ca_3(PO_4)_2$, and $Zn_5(OH)_6Cl_6H_2O$ after both static and dynamic immersion tests, with elevated intensity levels of these biodegradation products under the dynamic condition (Fig. 4g).

3.4. Reconstructed morphologies of the specimens after biodegradation

Under the static condition, the specimens underwent more localized biodegradation (Fig. 5a, yellow circles) than those under the dynamic one during the same period of 28 days. Interestingly, for the group S0402, the struts in the center seemed to experience more local biodegradation during the dynamic tests. In contrast, more biodegradation was found at the periphery of the specimens during the static tests.

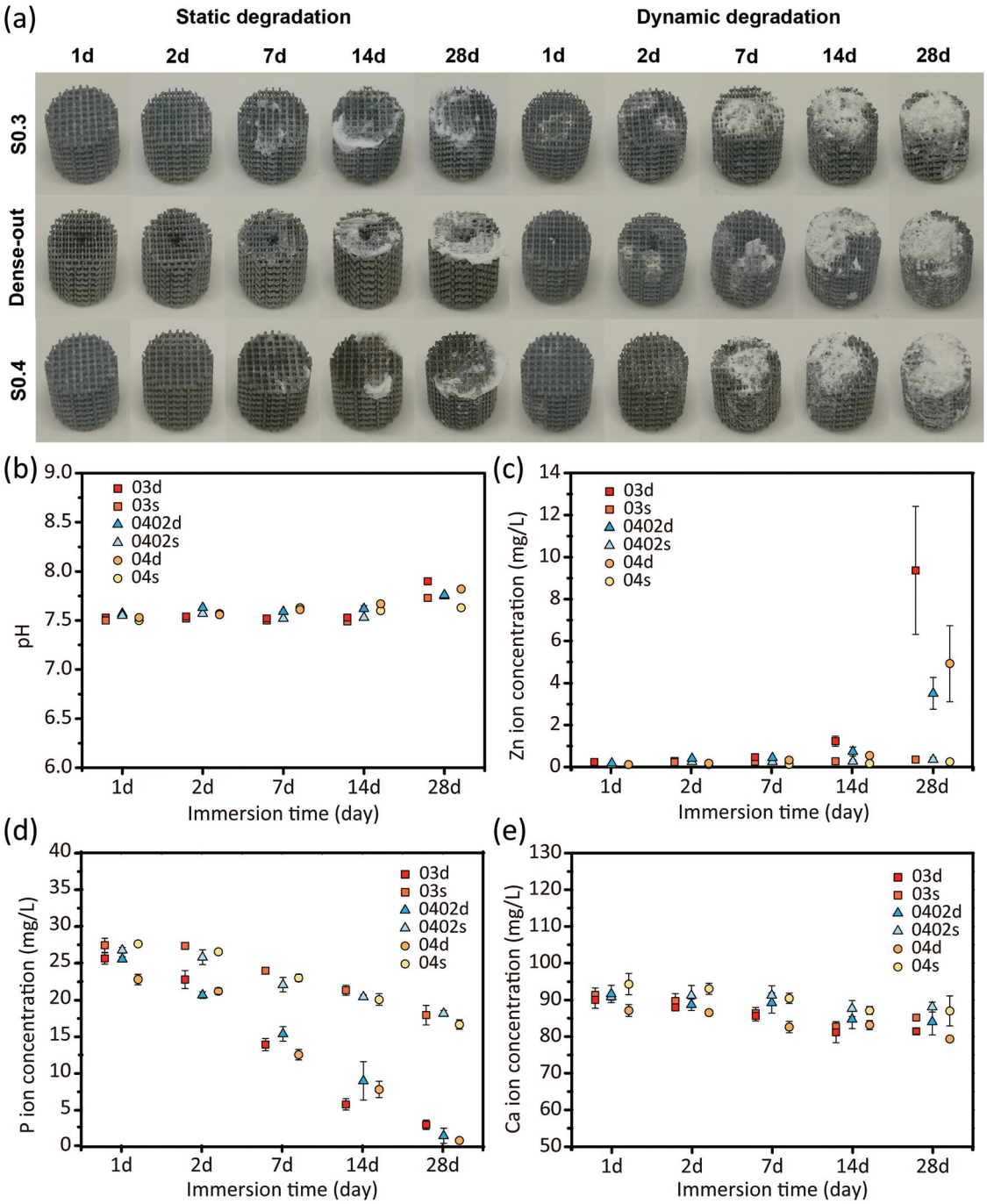

Fig. 3 Biodegradation behavior of AM porous Zn: (a) visual inspection of the as-degraded specimens under the static and dynamic conditions, (b) pH variation with the immersion time, (c–e) the changes in Zn (c), P (d), and Ca (e) ion concentrations with immersion time.

Furthermore, larger volumes of biodegradation products (Fig. 5a, red) formed during the dynamic immersion tests than during the static tests. The biodegradation products appeared to have mostly formed on a specific side of the specimens, which was further dependent on the testing condition (Fig. 5a). Under the static condition, the biodegradation products mainly formed at the bottom side of the specimens, which was in contact with the beaker (Fig. 5a). Under the dynamic condition, however, the biodegradation products were found mostly on the top side of the specimens, which was the outlet side of the r-SBF flow (Fig. 5a). After 28 days of dynamic biodegradation, specimens of the groups S03 and S04 exhibited the highest (11.9% ± 0.6%) and lowest (7.1% ± 0.3%) values of volume reduction, respectively (Fig. 5b). The volume loss of the specimens of the group S0402 was in-between those extreme values (7.9% ± 0.6%) (Fig. 5b). As compared to the dynamic biodegradation tests, the static ones resulted in considerably lower values of volume loss in all the groups

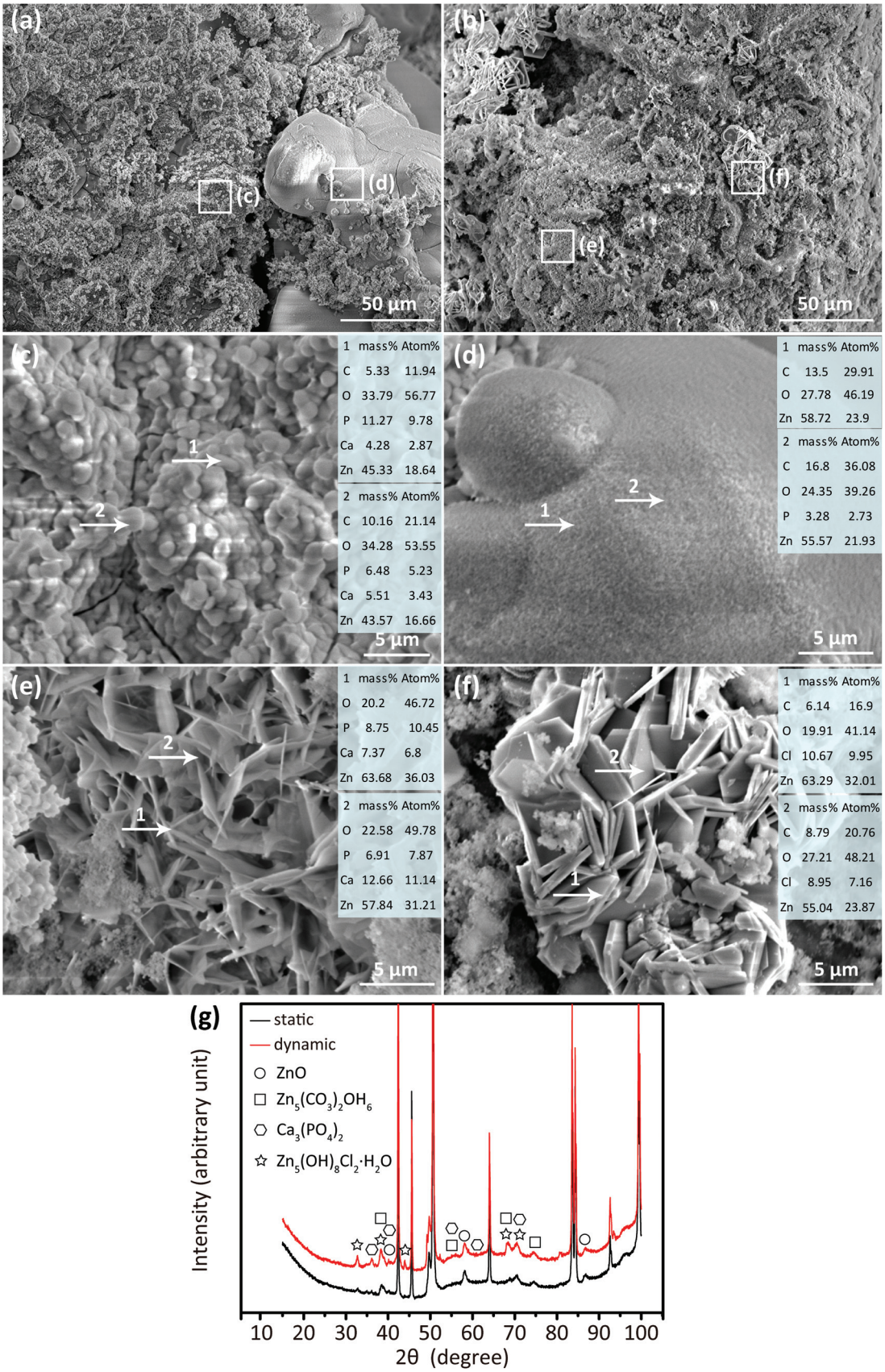

Fig. 4 Biodegradation products of AM porous Zn at lower (a–b) and higher (c–f) magnification: (c) particle-like biodegradation products, (d) dome-like biodegradation products, (e) needle-like biodegradation products, (f) flake-like biodegradation products, and (g) XRD analysis.

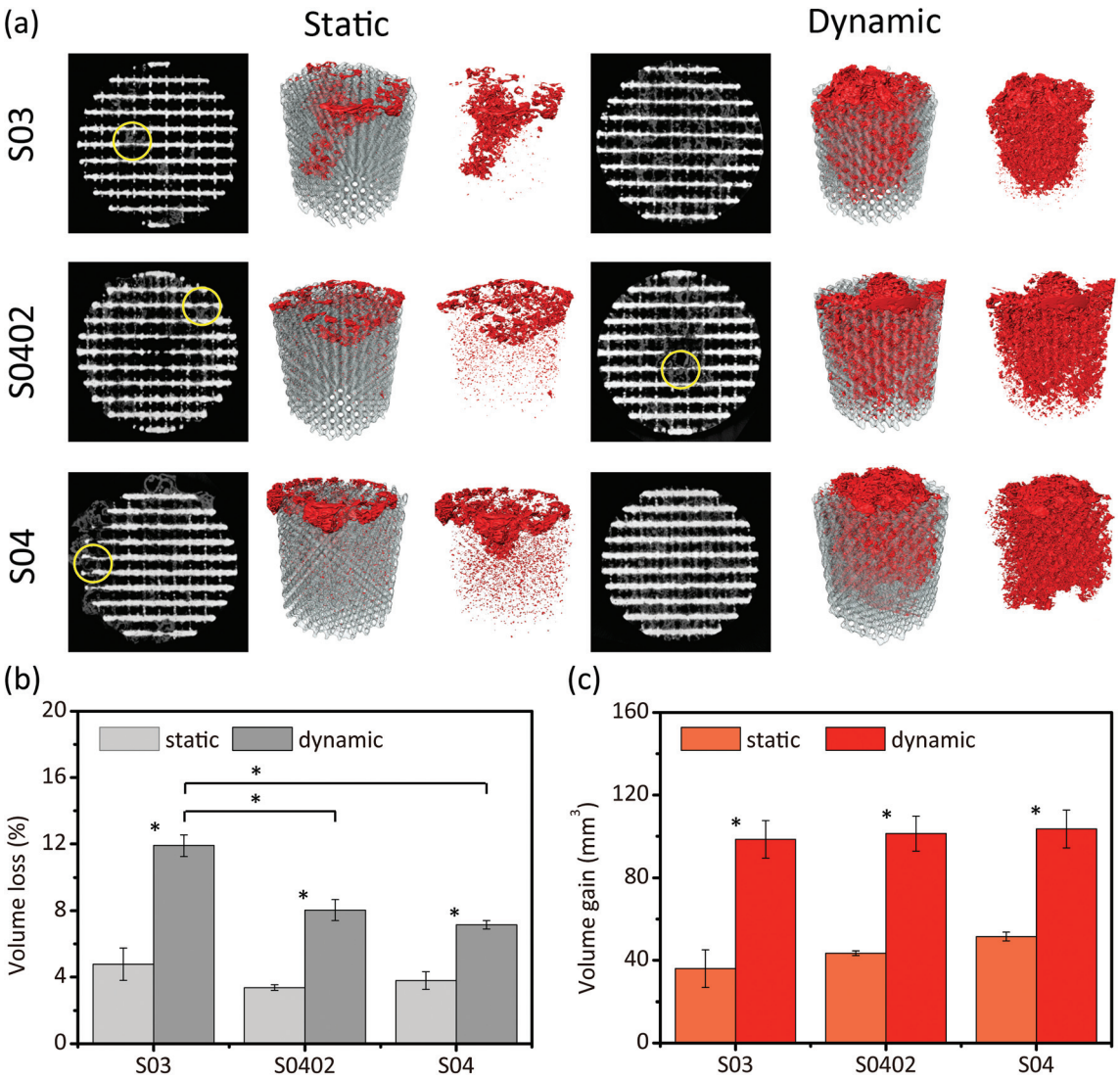

Fig. 5 Micro-CT analysis of AM porous Zn after 28 days of biodegradation: (a) 3D reconstruction, (b) volume losses of AM porous Zn, and (c) volume gains due to the formation of the biodegradation products shown in Fig. 4. Grey: Zn. Red: biodegradation products. Circle: localized biodegradation.

(Fig. 5b). The dynamic tests resulted in about twice as much biodegradation product volumes (*i.e.*, volume gain) in all the three experimental groups, as compared to the static tests (Fig. 5c).

3.5. Mechanical properties and their changes with biodegradation time

The specimens from all the experimental groups exhibited smooth stress–strain curves under compression, even after *in vitro* biodegradation for 28 days (Fig. 6a and b). The stress–strain curves of the three groups all exhibited a linear elastic region at early stage, followed by a gradually decreasing slope until a plateau stage, and rapidly increased stresses towards the end (Fig. 6a and b).

Among the as-built specimens, those of the S04 group possessed the highest elastic modulus (785.7 ± 72.1 MPa) and yield strength (10.8 ± 0.2 MPa), whereas the S03 group showed the lowest elastic modulus (399.8 ± 32.3 MPa) and yield strength (4.2 ± 0.1 MPa) (Fig. 6c and d). Functionally graded group specimens (S0402) had the mechanical properties in between those of the S03 and S04 groups (Fig. 6c and d). After 1 day of biodegradation, the elastic moduli and yield strengths of the specimens of all the groups increased (Fig. 6c and d). Thereafter, all the groups showed fluctuations in elastic modulus (Fig. 6c), while their yield strengths gradually increased with immersion time (Fig. 6d). All the groups showed higher yield strengths at day 28 as compared to those of the corresponding as-built specimens (Fig. 6d). In addition, the specimens that had undergone dynamic biodegradation exhibited higher yield strengths, as compared to those exposed to the static condition (Fig. 6d).

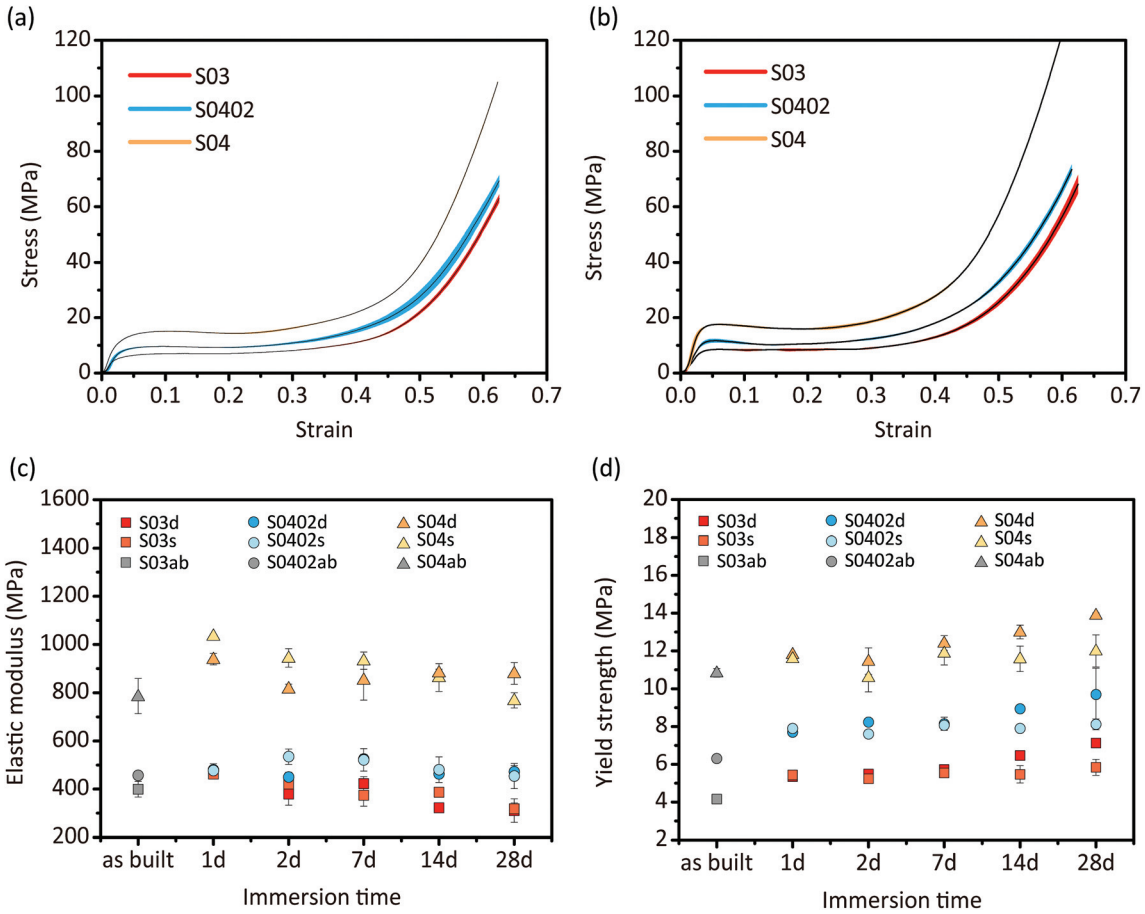

Fig. 6 Compressive stress–strain curves of the AM porous Zn specimens before (a) and after (b) 28 days of degradation as well as the changes in elastic modulus (c) and yield strength (d) with immersion time.

3.6. Permeability and cell seeding efficiency

The order of the AM porous Zn specimens from the highest permeability to the lowest value was as follows: S03, S0402, and S04 (Fig. 7a). The cell seeding efficiencies (Fig. 7b) measured for all the experimental groups were above 70%: S03 (75.2%), S0402 (74.35%), and S04 (87.85%) (Fig. 7b). Interestingly, specimens of the group S04 showed a 12% increase in cell seeding efficiency in comparison to those of the S03 group, while the seeding efficiency of the functionally graded structure (S0402) did not significantly differ from that of the group S03 (Fig. 7b).

3.7. *Direct* evaluation of cytocompatibility

The assessment of direct contact cytocompatibility by live-dead staining revealed that most of MG-63 cells were viable

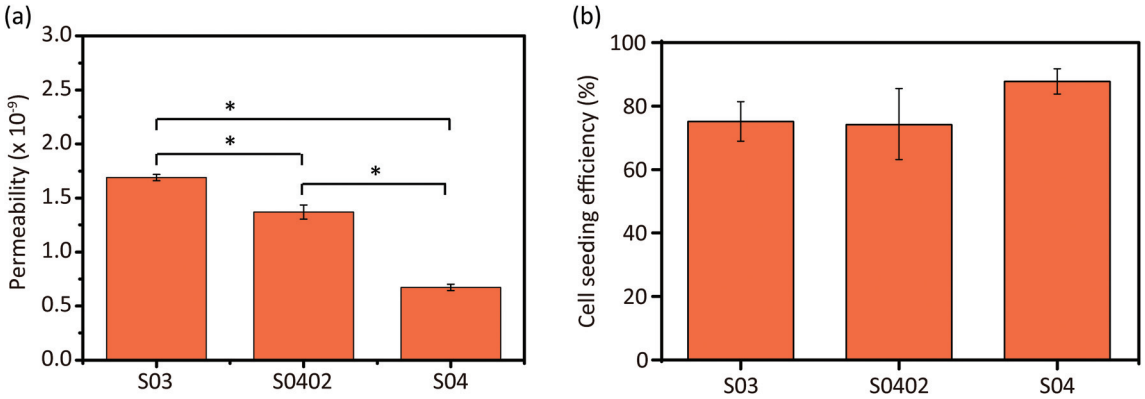

Fig. 7 Permeability values (a) and cell seeding efficiency values (b) of the AM porous Zn specimens of all the three experimental groups.

(fluorescing green) and only a few cells exhibited evidence of a compromised cell membrane integrity (fluorescing yellow-red) after 24 h of direct contact with the AM porous Zn specimens (Fig. 8a–f). Adhered cells were observed at the periphery as well as at the center of the Zn specimens (Fig. 8d–f), as is evident from these cross-sectional images. S04 and S0402 specimens appeared to contain more cells as compared to S03 specimen (Fig. 8a–f). The functional gradient in strut thickness (*i.e.*, S0402 group) did not seem to influence the regional distribution of cells within the scaffold (Fig. 8d–f).

3.8. Indirect biocompatibility *in vitro*

Cytocompatibility of the novel Zn specimens was assessed quantitatively using standardized extracts, and compared to that of the Ti-6Al-4V control, as recommended by ISO 10993. Cell viability in the 24 h-extracts was higher than 95% for all the porous Zn specimens, regardless of the topological design: 99.08% (S03), 96.78% (S0402), and 97.83% (S04) (Fig. 8h–i). At all tested time points, up to harsh 72 h evaluation, the cell viability values found for the porous Zn groups were not signifi-

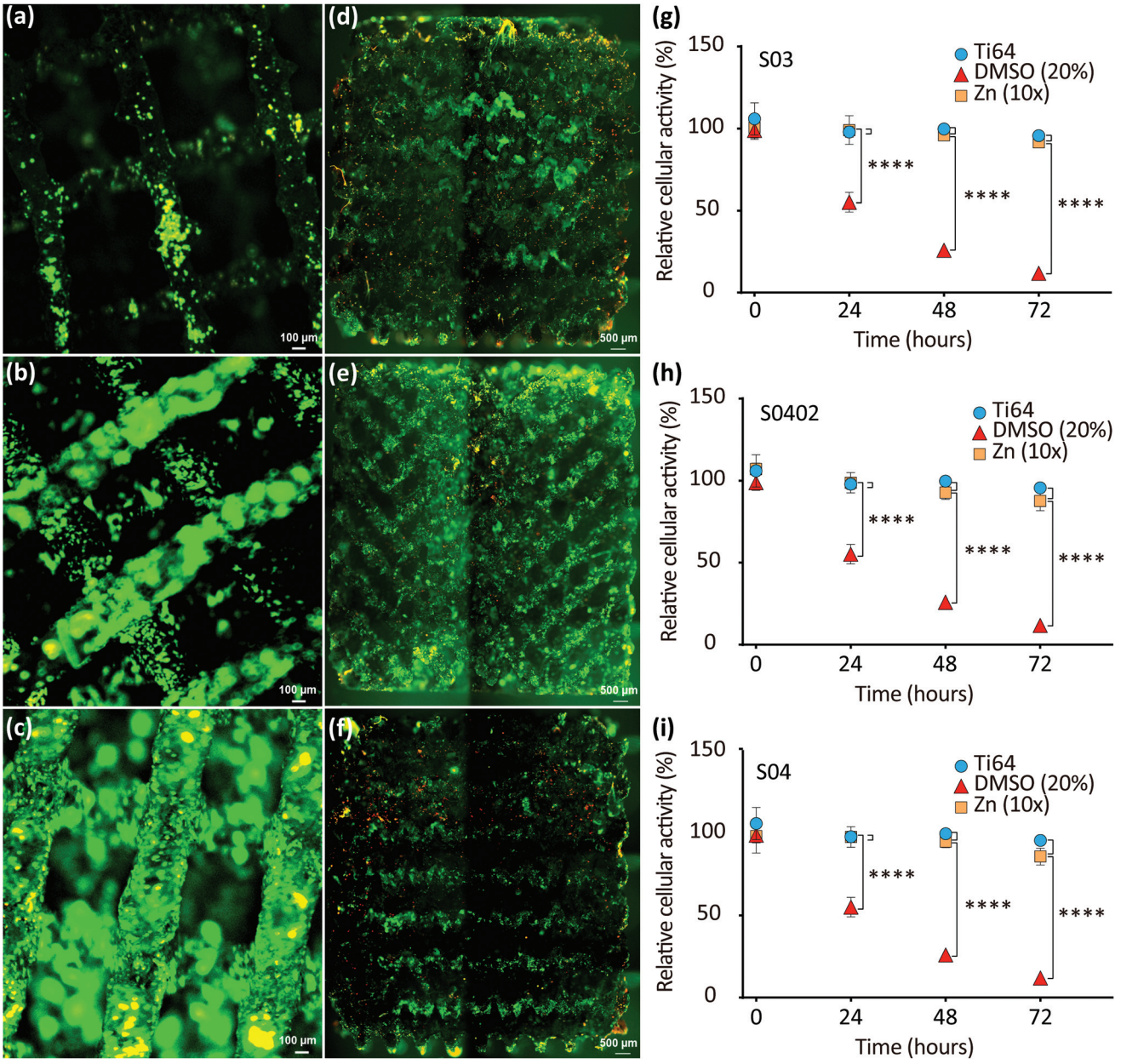

Fig. 8 Cytocompatibility of AM porous Zn: images of fluorescent cells attached on top of specimens from group S03 (a), S0402 (b), and S04 (c), respectively, next to cell distribution in cross-sections of the respective specimens S03 (d), S0402 (e), and S04 (f) to demonstrate homogenous seeding in the specimen's core. Relative cellular activities of MG-63 cells *in vitro* upon exposure to Zn scaffolds S03 (g), S0402 (h), and S04 (i) (n = 5). Randomly chosen scaffolds per group were tested in at least triplicates (Zn, n = 5; Ti-6Al-4V, n = 3).

cantly different from those found for the gold standard material (*i.e.*, Ti-6Al-4V) (Fig. 8h–i).

4. Discussion

Topological designs hold great promise for tuning the biodegradation behavior and mechanical properties of AM porous biodegradable metallic biomaterials. Here, we studied, for the first time ever, how topological design including a functional gradient can be applied to AM porous Zn. After biodegradation for 28 days, the volume losses of the AM porous Zn specimens varied between 7% to 12% (*i.e.*, 0.13–0.17 mm per year), depending on the topological design, suggesting that we could exploit the topological design to achieve a desired value of biodegradation rate. Interestingly and being contrary to other AM porous biodegradable metals,[5,6] the yield strengths of the specimens of all the groups increased after 28 days of immersion. Furthermore, the specimens of all the groups showed excellent cytocompatibility, regardless of the topological design. The results demonstrate that AM porous Zn, with appropriate design, holds great potential to fulfill the multiple and often conflicting requirements that are laid out for an ideal bone substitute.

4.1. Biodegradation behavior

Based on the SEM/EDS analysis, the flake-like biodegradation products could be $Zn_5(OH)_8Cl_2{\cdot}H_2O$ (Fig. 4f),[28] while the dome-like biodegradation products were most likely $Zn_5(CO_3)_2(OH)_6$ (Fig. 4d).[29] Higher percentages of Ca and P elements were found in the clusters of small particles (Fig. 4c), which could be hydroxyapatite or a combination of ZnO and $Ca_3(PO_4)_2$.[30] This confirmed the results of the ICP analysis, showing that the concentrations of P and Ca ions gradually decreased with immersion time, as these ions were involved in the growth of the biodegradation products (Fig. 3d and e). Furthermore, at all immersion time points and for all the experimental groups, the specimens that had undergone dynamic biodegradation exhibited higher Zn ion concentrations, but lower P and Ca ion concentrations in the immersion medium, as compared to the specimens exposed to the static biodegradation testing. This can be attributed to more biodegradation products formed under the dynamic testing condition (Fig. 3a). Under the dynamic condition, the surface of the AM porous Zn specimens was constantly washed by the medium. The flow of the medium over the surface of the specimen inhibited the increase of local pH, thereby increasing the rate of biodegradation[31] and the rate of the formation of the biodegradation products. The human body has a constant pH around 7.4.[32] Furthermore, the interstitial fluid flows through the (intra) medullary cavities at a rate of 0.012–1.67 ml min^{-1}.[33] Therefore, the dynamic biodegradation setup used in this research can mimic some aspects of the *in vivo* environment.

Under the static condition, no large differences were found between the three experimental groups with respect to Zn ion release into the medium (Fig. 3c). In contrast, the dynamic tests showed that, after 28 days, a higher Zn ion concentration was found for the specimens of the group S03 than those of the groups S04 and S0402. Moreover, the pH value of the group S03 was slightly higher compared to the other two groups (Fig. 3b). Micro-CT results confirmed that the volume losses of the AM porous Zn relied strongly on the topological design, with the group S03 exhibiting the largest volume loss. Topological design changed the permeability (*i.e.*, the fluid flow inside the scaffolds) and thus influenced the biodegradation profile of the AM porous Zn. Generally, a higher porosity leads to a higher permeability and a higher rate of material loss during the *in vitro* immersion tests. Therefore, the biodegradation behavior of AM Zn scaffolds can be effectively tuned by modifying the topological design of the porous structures.

Besides the commonly observed biodegradation behavior of AM porous Zn, micro-CT analysis suggested that the specimens experienced more localized biodegradation under the static condition (Fig. 5a). Moreover, localized biodegradation mainly occurred at the bottom of the specimens. This phenomenon was likely caused by the stagnant flow of r-SBF entrapped in the narrow gap between the specimens and the beaker. Cl^- likely accumulated at these locations and may form a local passive layer inside those narrow spaces.[34] Pitting or crevice-like biodegradation would then take place. On the contrary, dynamic flow prevented the adsorption of Cl^- on the surface of the degraded layer, thereby ensuring the homogeneity of the biodegradation process.[31,35] Interestingly, under the dynamic condition, localized biodegradation occurred at the core of the S0402 specimens, which could be related to the velocity distribution introduced by the gradient design. According to the computational fluid dynamics (CFD) simulations reported in a previous paper of the present authors,[10] the S0402 specimens have a relatively higher flow velocity at the center than on the periphery. It can then be inferred that varied biodegradation rates within one single scaffold can be achieved simultaneously by tuning the local porosity (*i.e.*, the permeability). Under the static condition, however, the group S0402 experienced more localized biodegradation at the periphery, where the struts were thicker and pores were smaller. The smaller pores in the graded structure may increase the possibility for localized degradation to occur. The differences between the static and dynamic conditions in terms of biodegradation rate and biodegradation mechanism observed at different locations within the specimens underscore the fact that, besides the choice of the biomaterial, the topological design of the porous structure plays a crucial role in controlling the biodegradation profile of the resulting implants.

The rates of Zn biodegradation found in this research are comparable (*i.e.*, 0.06–0.07 mm per year under the static condition and 0.13–0.17 mm per year under the dynamic condition) with the biodegradation rates reported by others (*i.e.*, 0.011–0.084 mm per year under static conditions[30,36,37]). Compared with the static biodegradation rate of AM porous Mg (0.23 mm per year) and Fe scaffolds (0.03 mm per year),[5,6]

AM porous Zn showed a moderate degradation profile in between. Furthermore, it is interesting to note that, for pure Zn, the results from *in vitro* biodegradation tests are largely consistent with those found *in vivo* (*i.e.*, 0.010–0.065 mm per year).[38–44] It should, however, be noted that in most *in vivo* tests, pure Zn wires or stents that were used for those measurements were implanted in the abdominal aorta. Based on these considerations, AM porous Zn exhibited a moderate biodegradation rate that corresponds to complete degradation within 1–2 years.[45] However, in the future, animal experiments with AM porous Zn should be performed to determine its, possibly implantation site-specific, real *in vivo* biodegradation rate in order to better predict its potential as a bone substituting material and its local tissue responses.

4.2. Mechanical behavior

All the AM Zn scaffolds, even after 28 days of biodegradation, still had the mechanical properties within the scope of those of cancellous bone (E = 0.01–2 GPa, σ_y = 0.2–80 MPa (ref. 2)) (Fig. 6). Similarly to AM porous Fe, titanium, and tantalum,[5,10,46,47] the AM porous Zn specimens had smooth stress–strain curves a plateau stage (Fig. 6a and b), which could be attributed to the high ductility of pure Zn.[21] Regarding the functionally graded design (S0402), as the struts thickness continuously and gradually changed, abrupt changes in stress at the boundary between different struts could be minimized.[48] In the case of the three different groups, porosity strongly affected the elastic modulus and yield strengths of the AM Zn specimens: lower porosity resulted in a higher elastic modulus and yield strength. As the porosity of the group S0402 fell between the porosities of the S03 and S04 groups, their mechanical properties were also in between those of the S03 and S04 groups. Generally, human bone has a highly anisotropic and heterogeneous structure, leading to different strength and stiffness values in different directions and at different locations.[49] Meanwhile, bone has a sufficient permeability in order to transfer nutrients and cells. Therefore, biodegradable porous bone-substituting implants should also have a tailored distribution of mechanical properties and a certain range of permeability values. In this study, with a linearly and radially graded design, we attempted to show that it was possible to achieve those goals to some extent.

After one day of *in vitro* biodegradation, specimens of all the three groups showed improved mechanical properties as compared to those of their as-built counterparts. Although similar results were found at the early stages of the biodegradation of AM porous Mg and Fe,[5,6] the mechanical properties of the biodegraded specimens S0402 and S04 were higher than those of their as-built counterparts, even after *in vitro* biodegradation for 28 days (Fig. 6c and d). Interestingly, the specimens subjected to dynamic biodegradation had higher yield strengths as compared to those under the static condition. The increases in the mechanical properties of the biodegradable metal with immersion time could be attributed to the contributions of the biodegradation products. AM porous Zn may behave like a composite material consisting of Zn and the biodegradation products. As shown in our previous study, the micro hardness of the biodegradation products was almost 5 times as high as the AM Zn.[24] The hardness can be converted approximately to strength, although the ratio varies from ductile metal to brittle ceramic over a wide range.[50] While progressing biodegradation deteriorated the mechanical properties of Zn, the formation of large amounts of biodegradation products under the dynamic condition could help in retaining, or even improving its mechanical properties. Under the static condition, however, a smaller volume of biodegradation products was less effective in playing this role and more localized biodegradation led to decreases in yield strength.

These observations, together with the bone-mimicking mechanical properties suggest that AM porous Zn is a promising candidate for orthopedic implants. Of course, animal experiments will still be required to see how far the here reported changes in mechanical properties *in vitro* can be translated into the *in vivo* situation. Of note, the mechanical properties of AM porous Zn may also change as a result of bone tissue regeneration.[51] These two effects (*i.e.*, Zn biodegradation *vs.* bone tissue neoformation) should be simultaneously considered when studying the evolution of the mechanical properties of such biomaterials with time. Computational models of degradation and bone tissue growth could be also used to predict the mechanical performance of biodegradable metals.[52] Moreover, no information is available yet concerning the fatigue behavior of these biomaterials. Given the fact that both topological design and material category significantly affect both the static and dynamic mechanical behaviors of AM porous metallic biomaterials,[53–56] there is a need for a thorough study on the dynamic mechanical responses of these porous structures.[57]

4.3. Cytocompatibility

The ISO 10993-recommended MTS assay, which is a sensitive and quantitative method to colorimetrically identify viable cells, revealed no significant differences in cellular activities of MG-63 indicator cells between the three different structures (*i.e.*, S03, S0402, and S04). All the three groups revealed a good cytocompatibility. While Zn ions at low concentrations hold potential to enhance cell viability, adhesion, proliferation, and migration,[58] at high concentrations they may stimulate oxidative stress pathways, inducing cell apoptosis and necrosis.[59] However, *in vivo* the body's vasculature facilitates the removal of Zn ions and respective biodegradation products, which helps prevent detrimental local ion overloads. Therefore, we used recently recommended modification to the ISO 10993 standards to make them applicable for absorbable biomaterials.[60] Using the suggested 10× diluted extracts in indirect cytotoxicity assays, the group S04 revealed 85% cellular activity, which was the lowest among all the groups, while the S03 specimens showed the highest (*i.e.*, 91%) cellular activity, after relatively harsh 72 h incubation. Of note, during more frequently reported 24 to 48 h incubation times, cellular activities remained >90% in all the tested extracts. Thus, the Zn extracts

from all the three experimental groups may be considered to be non-toxic (*i.e.*, 75–99% viability; cytotoxicity grade 1). Although a higher porosity normally increases permeability, thereby resulting in greater ion release into extracts,[20,40] the outcome of our study did not indicate such differences between the three experimental groups. However, while our cytocompatibility testing regime was in line with current ISO 10993 recommendations,[60] even our longest immersion time might have been too short to fully appreciate such increases in ion release, which may require weeks to occur.

To better appreciate any cell to biomaterial contact-mediated cytocompatibility issues, we additionally performed cell seeding experiments with all the three different AM porous Zn scaffolds using semi-quantitative fluorescent live/dead imaging. 24 h after seeding, majority of MG-63 cells remained viable and appeared well attached to the specimen surfaces. Interestingly, Zn-based biomaterials have been shown to support, among others, cell viability and proliferation, because Zn ions are important cofactors in a variety of metabolic processes.[61] From surface visualization and cross-sectional imaging, MG-63 cells appeared to be evenly distributed along the periphery as well as within the core region of the specimens, without showing any obvious design-related differences. It is in agreement with the results obtained by other researchers who analyzed pre-osteoblasts in graded Ti-6Al-4V scaffolds,[62] in comparison with cell distribution in graded polymer 3D scaffolds.[63] Of note, cell seeding efficiency was above 70% (*i.e.*, 70% cells attached to the Zn surface) for all the three porous Zn scaffold designs, but a slightly higher efficacy in the group S04 was noticed, as compared to S03. Fluorescent images also showed that S04 and S0402 specimens appeared to contain more attached cells as compared to S03 specimen (Fig. 8a–f). A general expectation may be that a smaller pore size provides a larger strut surface area for cell–surface interactions before cells pass through the pores. In addition, pore-clogging may result in increased cell accumulation within the scaffold.[64] However, with fluorescence it was hard to quantify cells objectively and the AM Zn scaffolds did not show significant differences in cell seeding efficiency between the different groups. A possible explanation might be that the scaffolds designed in the present study were graded along the radial direction (*i.e.*, along the *x* and *y* axes), instead of the axial direction (*z*-axis), as in other studies.[64–66] Axial gradation could create a "sieve effect" during cell seeding and may account for increased cell seeding efficiencies. Another likely reason is that the pore/strut size differences between the scaffolds in our study were not large enough to significantly influence cell seeding efficiency. Moreover, fluorescent imaging has its limitations and is difficult to quantify within opaque metal 3D structures, which is a limitation of the present study.

5. Conclusions

We demonstrated that functionally graded porous Zn with precisely controlled topology can be fabricated by using PBF and the biodegradation behavior and mechanical properties of AM porous Zn can be tuned through topological design. The topological design changed the permeability by up to 3-fold and altered the biodegradation rate by up to 1.5-fold between the 3 groups of the AM porous Zn. Of note, the biodegradation rates of all the groups of AM porous Zn were rather moderate, with 7.1%–11.9% volume losses after 28 days of dynamic *in vitro* biodegradation. Elastic modulus (400–786 MPa) and yield strengths (4–11 MPa) of the specimens of all the three groups remained within the scope of those of human cancellous bone. Regardless of the topological design, the AM porous Zn exhibited good biocompatibility *in vitro*. The results highlighted that proper topological design plays an important role in developing AM biodegradable porous metals. AM porous Zn holds great potential for bone substitution in the future.

Conflicts of interest

There are no conflicts to declare.

Acknowledgements

The authors are grateful for the financial support from the Prosperos project, funded by the Interreg VA Flanders – The Netherlands program, CCI Grant No. 2014TC16RFCB04. Y. L. thanks the China Scholarship Council (CSC) for financial support. K. L. thanks VLAIO (Flanders Agency for Innovation and Entrepreneurship) for the financial support (IWT140257). Richard Huizenga at the Department of Materials Science and Engineering, Delft University of Technology, is acknowledged for the XRD analysis.

References

1 A. H. Yusop, A. A. Bakir, N. A. Shaharom, M. R. Abdul Kadir and H. Hermawan, Porous biodegradable metals for hard tissue scaffolds: a review, *Int. J. Biomater.*, 2012, **2012**, 10.
2 M. Yazdimamaghani, M. Razavi, D. Vashaee, K. Moharamzadeh, A. R. Boccaccini and L. Tayebi, Porous magnesium-based scaffolds for tissue engineering, *Mater. Sci. Eng., C*, 2017, **71**, 1253–1266.
3 R. Gorejová, L. Haverová, R. Oriňaková, A. Oriňak and M. Oriňak, Recent advancements in Fe-based biodegradable materials for bone repair, *J. Mater. Sci.*, 2019, **54**, 1913–1947.
4 A. A. Zadpoor, Additively manufactured porous metallic biomaterials, *J. Mater. Chem. B*, 2019, **7**, 4088–4117.
5 Y. Li, H. Jahr, K. Lietaert, P. Pavanram, A. Yilmaz, L. I. Fockaert, M. A. Leeflang, B. Pouran, Y. Gonzalez-Garcia, H. Weinans, J. M. C. Mol, J. Zhou and A. A. Zadpoor, Additively manufactured biodegradable porous iron, *Acta Biomater.*, 2018, **77**, 380–393.

6 Y. Li, J. Zhou, P. Pavanram, M. A. Leeflang, L. I. Fockaert, B. Pouran, N. Tümer, K. U. Schröder, J. M. C. Mol, H. Weinans, H. Jahr and A. A. Zadpoor, Additively manufactured biodegradable porous magnesium, *Acta Biomater.*, 2018, **67**, 378–392.

7 Y. F. Zheng, X. N. Gu and F. Witte, Biodegradable metals, *Mater. Sci. Eng., R*, 2014, **77**, 1–34.

8 Y. Yang, C. He, E. Dianyu, W. Yang, F. Qi, D. Xie, L. Shen, S. Peng and C. Shuai, Mg bone implant: Features, developments and perspectives, *Mater. Des.*, 2020, **185**, 108259.

9 D. Andreas, H. Thomas, B. F. Wilhelm and P. Matthias, In vitro and in vivo corrosion properties of new iron–manganese alloys designed for cardiovascular applications, *J. Biomed. Mater. Res., Part B*, 2015, **103**, 649–660.

10 Y. Li, H. Jahr, P. Pavanram, F. S. L. Bobbert, U. Puggi, X. Y. Zhang, B. Pouran, M. A. Leeflang, H. Weinans, J. Zhou and A. A. Zadpoor, Additively manufactured functionally graded biodegradable porous iron, *Acta Biomater.*, 2019, **96**, 646–661.

11 C. Gao, M. Yao, S. Li, P. Feng, S. Peng and C. Shuai, Highly biodegradable and bioactive Fe-Pd-bredigite biocomposites prepared by selective laser melting, *J. Adv. Res.*, 2019, **20**, 91–104.

12 D. Pierson, J. Edick, A. Tauscher, E. Pokorney, P. Bowen, J. Gelbaugh, J. Stinson, H. Getty, C. H. Lee, J. Drelich and J. Goldman, A simplified in vivo approach for evaluating the bioabsorbable behavior of candidate stent materials, *J. Biomed. Mater. Res., Part B*, 2012, **100**, 58–67.

13 L.-Y. Li, L.-Y. Cui, R.-C. Zeng, S.-Q. Li, X.-B. Chen, Y. Zheng and M. B. Kannan, Advances in functionalized polymer coatings on biodegradable magnesium alloys – A review, *Acta Biomater.*, 2018, **79**, 23–36.

14 Y. Zheng, X. Xu, Z. Xu, J. Wang and H. Cai, *Development of Fe-based degradable metallic biomaterials. Metallic Biomaterials*, Wiley-VCH Verlag GmbH & Co. KGaA, 2017, pp. 113–160.

15 J. Venezuela and M. S. Dargusch, The influence of alloying and fabrication techniques on the mechanical properties, biodegradability and biocompatibility of zinc: A comprehensive review, *Acta Biomater.*, 2019, **87**, 1–40.

16 L. Zhao, Z. Zhang, Y. Song, S. Liu, Y. Qi, X. Wang, Q. Wang and C. Cui, Mechanical properties and in vitro biodegradation of newly developed porous Zn scaffolds for biomedical applications, *Mater. Des.*, 2016, **108**, 136–144.

17 J. Niu, Z. Tang, H. Huang, J. Pei, H. Zhang, G. Yuan and W. Ding, Research on a Zn-Cu alloy as a biodegradable material for potential vascular stents application, *Mater. Sci. Eng., C*, 2016, **69**, 407–413.

18 C. Gao, M. Yao, C. Shuai, S. Peng and Y. Deng, Nano-SiC reinforced Zn biocomposites prepared via laser melting: Microstructure, mechanical properties and biodegradability, *J. Mater. Sci. Technol.*, 2019, **35**, 2608–2617.

19 C. Shuai, Y. Cheng, Y. Yang, S. Peng, W. Yang and F. Qi, Laser additive manufacturing of Zn-2Al part for bone repair: Formability, microstructure and properties, *J. Alloys Compd.*, 2019, **798**, 606–615.

20 X. Wang, X. Shao, T. Dai, F. Xu, J. G. Zhou, G. Qu, L. Tian, B. Liu and Y. Liu, In vivo study of the efficacy, biosafety, and degradation of a zinc alloy osteosynthesis system, *Acta Biomater.*, 2019, **92**, 351–361.

21 Y. Qin, P. Wen, M. Voshage, Y. Chen, P. G. Schückler, L. Jauer, D. Xia, H. Guo, Y. Zheng and J. H. Schleifenbaum, Additive manufacturing of biodegradable Zn-xWE43 porous scaffolds: Formation quality, microstructure and mechanical properties, *Mater. Des.*, 2019, **181**, 107937.

22 P. Wen, Y. Qin, Y. Chen, M. Voshage, L. Jauer, R. Poprawe and J. H. Schleifenbaum, Laser additive manufacturing of Zn porous scaffolds: Shielding gas flow, surface quality and densification, *J. Mater. Sci. Technol.*, 2019, **35**, 368–376.

23 K. Lietaert, B. Neirinck, J. Plas and J. Vleugels, *Influence of unit cell architecture and of relative density on the mechanical properties of additively manufactured Zn scaffolds as biodegradable implant materials. Proceedings Euro PM 2017: International Powder Metallurgy Congress and Exhibition*, The European Powder Metallurgy Association, Politecnico di Milano, Italy, 2017, pp. 1–7.

24 Y. Li, P. Pavanram, J. Zhou, K. Lietaert, P. Taheri, W. Li, H. San, M. A. Leeflang, J. M. C. Mol, H. Jahr and A. A. Zadpoor, Additively manufactured biodegradable porous zinc, *Acta Biomater.*, 2020, **101**, 609–623.

25 K. Lietaert, W. Baekelant, L. Thijs and J. Vleugels, *Direct metal printing of zinc: from single laser tracks to high density parts. European Congress and Exhibition on Powder Metallurgy. European PM Conference Proceedings, Swerea KIMAB*, The European Powder Metallurgy Association, Sweden, 2016, pp. 1–6.

26 A. Oyane, H.-M. Kim, T. Furuya, T. Kokubo, T. Miyazaki and T. Nakamura, Preparation and assessment of revised simulated body fluids, *J. Biomed. Mater. Res., Part A*, 2003, **65**, 188–195.

27 K. Shimizu, A. Ito and H. Honda, Enhanced cell-seeding into 3D porous scaffolds by use of magnetite nanoparticles, *J. Biomed. Mater. Res., Part B*, 2006, **77**, 265–272.

28 M. M. Alves, L. M. Marques, I. Nogueira, C. F. Santos, S. B. Salazar, S. Eugénio, N. P. Mira and M. F. Montemor, In silico, in vitro and antifungal activity of the surface layers formed on zinc during this biomaterial degradation, *Appl. Surf. Sci.*, 2018, **447**, 401–407.

29 K. Törne, A. Örnberg and J. Weissenrieder, Influence of strain on the corrosion of magnesium alloys and zinc in physiological environments, *Acta Biomater.*, 2017, **48**, 541–550.

30 L. Liu, Y. Meng, C. Dong, Y. Yan, A. A. Volinsky and L.-N. Wang, Initial formation of corrosion products on pure zinc in simulated body fluid, *J. Mater. Sci. Technol.*, 2018, **34**, 2271–2282.

31 J. Lévesque, H. Hermawan, D. Dubé and D. Mantovani, Design of a pseudo-physiological test bench specific to the development of biodegradable metallic biomaterials, *Acta Biomater.*, 2008, **4**, 284–295.

32 J. C. Atherton, Acid–base balance: maintenance of plasma pH, *Anaesth. Intensive Care*, 2009, **10**, 557–561.
33 A. P. Md Saad and A. Syahrom, Study of dynamic degradation behaviour of porous magnesium under physiological environment of human cancellous bone, *Corros. Sci.*, 2018, **131**, 45–56.
34 H. Wu, C. Zhang, T. Lou, B. Chen, R. Yi, W. Wang, R. Zhang, M. Zuo, H. Xu, P. Han, S. Zhang, J. Ni and X. Zhang, Crevice corrosion – A newly observed mechanism of degradation in biomedical magnesium, *Acta Biomater.*, 2019, **98**, 152–159.
35 Y. Zong, G. Yuan, X. Zhang, L. Mao, J. Niu and W. Ding, Comparison of biodegradable behaviors of AZ31 and Mg–Nd–Zn–Zr alloys in Hank's physiological solution, *Mater. Sci. Eng., B*, 2012, **177**, 395–401.
36 X. Liu, J. Sun, F. Zhou, Y. Yang, R. Chang, K. Qiu, Z. Pu, L. Li and Y. Zheng, Micro-alloying with Mn in Zn–Mg alloy for future biodegradable metals application, *Mater. Des.*, 2016, **94**, 95–104.
37 M. Sikora-Jasinska, E. Mostaed, A. Mostaed, R. Beanland, D. Mantovani and M. Vedani, Fabrication, mechanical properties and in vitro degradation behavior of newly developed ZnAg alloys for degradable implant applications, *Mater. Sci. Eng., C*, 2017, **77**, 1170–1181.
38 P. K. Bowen, J. Drelich and J. Goldman, Zinc exhibits ideal physiological corrosion behavior for bioabsorbable stents, *Adv. Mater.*, 2013, **25**, 2577–2582.
39 A. Kafri, S. Ovadia, G. Yosafovich-Doitch and E. Aghion, In vivo performances of pure Zn and Zn–Fe alloy as biodegradable implants, *J. Mater. Sci.: Mater. Med.*, 2018, **29**, 94.
40 H. Yang, C. Wang, C. Liu, H. Chen, Y. Wu, J. Han, Z. Jia, W. Lin, D. Zhang, W. Li, W. Yuan, H. Guo, H. Li, G. Yang, D. Kong, D. Zhu, K. Takashima, L. Ruan, J. Nie, X. Li and Y. Zheng, Evolution of the degradation mechanism of pure zinc stent in the one-year study of rabbit abdominal aorta model, *Biomaterials*, 2017, **145**, 92–105.
41 A. J. Drelich, S. Zhao, R. J. Guillory, J. W. Drelich and J. Goldman, Long-term surveillance of zinc implant in murine artery: Surprisingly steady biocorrosion rate, *Acta Biomater.*, 2017, **58**, 539–549.
42 P. K. Bowen, R. J. Guillory, E. R. Shearier, J.-M. Seitz, J. Drelich, M. Bocks, F. Zhao and J. Goldman, Metallic zinc exhibits optimal biocompatibility for bioabsorbable endovascular stents, *Mater. Sci. Eng., C*, 2015, **56**, 467–472.
43 S. Zhao, J.-M. Seitz, R. Eifler, H. J. Maier, R. J. Guillory, E. J. Earley, A. Drelich, J. Goldman and J. W. Drelich, Zn-Li alloy after extrusion and drawing: Structural, mechanical characterization, and biodegradation in abdominal aorta of rat, *Mater. Sci. Eng., C*, 2017, **76**, 301–312.
44 A. A. Shomali, R. J. Guillory, D. Seguin, J. Goldman and J. W. Drelich, Effect of PLLA coating on corrosion and biocompatibility of zinc in vascular environment, *Surf. Innovations*, 2017, **5**, 211–220.
45 G. Jia, C. Chen, J. Zhang, Y. Wang, R. Yue, B. J. C. Luthringer - Feyerabend, R. Willumeit-Roemer, H. Zhang, M. Xiong, H. Huang, G. Yuan and F. Feyerabend, In vitro degradation behavior of Mg scaffolds with three-dimensional interconnected porous structures for bone tissue engineering, *Corros. Sci.*, 2018, **144**, 301–312.
46 R. Wauthle, J. van der Stok, S. Amin Yavari, J. Van Humbeeck, J.-P. Kruth, A. A. Zadpoor, H. Weinans, M. Mulier and J. Schrooten, Additively manufactured porous tantalum implants, *Acta Biomater.*, 2015, **14**, 217–225.
47 R. Wauthle, S. M. Ahmadi, S. Amin Yavari, M. Mulier, A. A. Zadpoor, H. Weinans, J. Van Humbeeck, J.-P. Kruth and J. Schrooten, Revival of pure titanium for dynamically loaded porous implants using additive manufacturing, *Mater. Sci. Eng., C*, 2015, **54**, 94–100.
48 X.-Y. Zhang, G. Fang, S. Leeflang, A. A. Zadpoor and J. Zhou, Topological design, permeability and mechanical behavior of additively manufactured functionally graded porous metallic biomaterials, *Acta Biomater.*, 2019, **84**, 437–452.
49 X. Wang, S. Xu, S. Zhou, W. Xu, M. Leary, P. Choong, M. Qian, M. Brandt and Y. M. Xie, Topological design and additive manufacturing of porous metals for bone scaffolds and orthopaedic implants: A review, *Biomaterials*, 2016, **83**, 127–141.
50 P. Zhang, S. X. Li and Z. F. Zhang, General relationship between strength and hardness, *Mater. Sci. Eng., A*, 2011, **529**, 62–73.
51 R. Hedayati, S. Janbaz, M. Sadighi, M. Mohammadi-Aghdam and A. A. Zadpoor, How does tissue regeneration influence the mechanical behavior of additively manufactured porous biomaterials?, *J. Mech. Behav. Biomed. Mater.*, 2017, **65**, 831–841.
52 A. A. Zadpoor, Meta-biomaterials, *Biomater. Sci.*, 2020, **8**, 18–38.
53 Y. Li, H. Jahr, X. Y. Zhang, M. A. Leeflang, W. Li, B. Pouran, F. D. Tichelaar, H. Weinans, J. Zhou and A. A. Zadpoor, Biodegradation-affected fatigue behavior of additively manufactured porous magnesium, *Addit. Manuf.*, 2019, **28**, 299–311.
54 Y. Li, K. Lietaert, W. Li, X. Y. Zhang, M. A. Leeflang, J. Zhou and A. A. Zadpoor, Corrosion fatigue behavior of additively manufactured biodegradable porous iron, *Corros. Sci.*, 2019, **156**, 106–116.
55 R. Hedayati, S. M. Ahmadi, K. Lietaert, B. Pouran, Y. Li, H. Weinans, C. D. Rans and A. A. Zadpoor, Isolated and modulated effects of topology and material type on the mechanical properties of additively manufactured porous biomaterials, *J. Mech. Behav. Biomed. Mater.*, 2018, **79**, 254–263.
56 S. M. Ahmadi, R. Hedayati, Y. Li, K. Lietaert, N. Tümer, A. Fatemi, C. D. Rans, B. Pouran, H. Weinans and A. A. Zadpoor, Fatigue performance of additively manufactured meta-biomaterials: The effects of topology and material type, *Acta Biomater.*, 2018, **65**, 292–304.
57 G. Li, H. Yang, Y. Zheng, X.-H. Chen, J.-A. Yang, D. Zhu, L. Ruan and K. Takashima, Challenges in the use of zinc and its alloys as biodegradable metals: Perspective from biomechanical compatibility, *Acta Biomater.*, 2019, **97**, 23–45.

58 J. Ma, N. Zhao and D. Zhu, Bioabsorbable zinc ion induced biphasic cellular responses in vascular smooth muscle cells, *Sci. Rep.*, 2016, **6**, 26661.
59 G. Katarivas Levy, J. Goldman and E. Aghion, The prospects of zinc as a structural material for biodegradable Implants —a review paper, *Metals*, 2017, **7**, 402.
60 J. Wang, F. Witte, T. Xi, Y. Zheng, K. Yang, Y. Yang, D. Zhao, J. Meng, Y. Li, W. Li, K. Chan and L. Qin, Recommendation for modifying current cytotoxicity testing standards for biodegradable magnesium-based materials, *Acta Biomater.*, 2015, **21**, 237–249.
61 D. Zhu, Y. Su, M. L. Young, J. Ma, Y. Zheng and L. Tang, Biological Responses and Mechanisms of Human Bone Marrow Mesenchymal Stem Cells to Zn and Mg Biomaterials, *ACS Appl. Mater. Interfaces*, 2017, **9**, 27453–27461.
62 E. Onal, J. Frith, M. Jurg, X. Wu and A. Molotnikov, Mechanical Properties and In Vitro Behavior of Additively Manufactured and Functionally Graded Ti6Al4V Porous Scaffolds, *Metals*, 2018, **8**, 200.
63 A. Di Luca, B. Ostrowska, I. Lorenzo-Moldero, A. Lepedda, W. Swieszkowski, C. Van Blitterswijk and L. Moroni, Gradients in pore size enhance the osteogenic differentiation of human mesenchymal stromal cells in three-dimensional scaffolds, *Sci. Rep.*, 2016, **6**, 22898.
64 K. C. Nune, A. Kumar, R. D. K. Misra, S. J. Li, Y. L. Hao and R. Yang, Functional response of osteoblasts in functionally gradient titanium alloy mesh arrays processed by 3D additive manufacturing, *Colloids Surf., B*, 2017, **150**, 78–88.
65 Q. Zhang, H. Lu, N. Kawazoe and G. Chen, Pore size effect of collagen scaffolds on cartilage regeneration, *Acta Biomater.*, 2014, **10**, 2005–2013.
66 S. H. Oh, I. K. Park, J. M. Kim and J. H. Lee, In vitro and in vivo characteristics of PCL scaffolds with pore size gradient fabricated by a centrifugation method, *Biomaterials*, 2007, **28**, 1664–1671.